

Near-wall pressure fluctuations over noise reduction add-ons

Avallone, Francesco; van der Velden, Wouter; Merino Martinez, Roberto; Ragni, Daniele

DOI

[10.2514/6.2017-4171](https://doi.org/10.2514/6.2017-4171)

Publication date

2017

Document Version

Accepted author manuscript

Published in

23rd AIAA/CEAS Aeroacoustics Conference

Citation (APA)

Avallone, F., van der Velden, W., Merino Martinez, R., & Ragni, D. (2017). Near-wall pressure fluctuations over noise reduction add-ons. In *23rd AIAA/CEAS Aeroacoustics Conference: 5-9 June 2017, Denver, Colorado* Article AIAA 2017-4171 American Institute of Aeronautics and Astronautics Inc. (AIAA). <https://doi.org/10.2514/6.2017-4171>

Important note

To cite this publication, please use the final published version (if applicable).
Please check the document version above.

Copyright

Other than for strictly personal use, it is not permitted to download, forward or distribute the text or part of it, without the consent of the author(s) and/or copyright holder(s), unless the work is under an open content license such as Creative Commons.

Takedown policy

Please contact us and provide details if you believe this document breaches copyrights.
We will remove access to the work immediately and investigate your claim.

Near-wall pressure fluctuations over noise reduction add-ons

Francesco Avallone¹, Wouter van der Velden², Roberto Merino Martinez³, and Daniele Ragni⁴
Delft University of Technology, Kluyverweg 1, 2629HS, Delft, The Netherlands

The hydrodynamic pressure fluctuations over the suction side of a NACA 0018 airfoil with trailing-edge add-ons are obtained from integration of time-resolved stereoscopic particle image velocimetry data and compared to ones computed with the Lattice Boltzmann method. The airfoil is retrofitted with solid and slitted serrated trailing edges. Analysis of the data confirms that the intensity of the pressure fluctuations along the edge of the serrations decreases from the root to the tip. Spectra of the pressure fluctuations vary in the stream-wise direction, which might be caused by the shear at the edge of the serration and by the flow seeping through the empty space in-between them. Results from slitted serrations show that they enhance the intensity of the pressure fluctuations at the root, with critical repercussion on their effectiveness in noise reduction.

I. Introduction

Surface pressure fluctuations below the turbulent boundary-layer approaching the trailing edge of a wing are the most relevant flow parameters for the estimation of broadband airfoil self noise.^{1,2} Lowering the rotational speed of the wind turbine has often been adopted as a temporary solution to mitigate this source of noise. In fact, by exploiting the fifth-power proportionality of the scattered noise to the local relative Mach number,³ a slower turbine is also more silent. However, this obviously reduces the energy production of the machine. For this reason, research was focused on several passive noise-mitigation solutions, which could be easily installed with a relatively low effect on the overall turbine performance.⁴ Amongst the most simple ones, sinusoidal and sawtooth geometries⁴⁻⁸ are already installed at the trailing edge of many industrial wind turbines. More complicated geometries have been designed by employing slits,⁹ brushes,¹⁰ randomly⁹ and iron-shaped trailing edges.¹¹ Although these shapes have proven to reduce noise emissions with respect to the clean trailing-edge configuration, a huge difference subsists between the theoretical predicted noise-reduction intensity^{12,13} and the one effectively measured in field.⁴

One of the most important analytical models found in literature is the one of Howe¹² where the broadband noise-reduction due to the installation of solid serrated edges on a flat plate is estimated. Lyu *et al*¹³ further developed a new semi-analytical model applying the Schwarzschild method of propagation of the pressure fluctuations. Although closer to reality, the final result does not allow yet to explain some of the physical features already at zero angle of attack such as the characteristic *cross-over* frequency $St_\delta = f\delta/V_\infty \approx 1$ (based on the free-stream velocity V_∞ and boundary-layer thickness δ , from XFOIL)¹⁴ after which noise increases again. It was recently showed that one of the limitations of the theoretical model is the assumption of frozen turbulence along the serration length.^{7,8} As a matter of fact, the intensity of the pressure fluctuations and their spectra vary in the stream-wise direction.

Linking the velocity evolution along the serration to the change of the pressure spectrum is an experimental challenge. Such a link would require a combination and perhaps a synchronization of velocity and surface pressure measurements. Additionally, it is practically impossible to install pressure sensors on thin serrations without perturbing the flow.^{5,15} An alternative approach consists in estimating pressure from velocity in turbulent-boundary layers,^{16,17} by solving the Navier-Stokes momentum equation in the Poisson form. This particular technique typically

¹ PostDoc Researcher, AWEP Department, f.avallone@tudelft.nl, AIAA member.

² Currently Senior Aerospace Application Engineer at EXA GmbH, wouter@exa.com, AIAA Member.

³ PhD Candidate, ANCE Dept, r.merinomartinez@tudelft.nl, AIAA Student Member.

⁴ Assistant Professor, AWEP Department, d.ragni@tudelft.nl, AIAA member.

allows obtaining higher spatial resolution with respect to the one that can be achieved via surface microphone. This approach has been extensively used in presence of turbulent flow developing over a flat plate;¹⁸ however, almost no-study focuses on trailing-edge serrations where strong three-dimensional effects are present.

In the present work, pressure spectra along serrated and slitted trailing-edges are obtained from experimental results at different wall-normal locations. They are compared with theoretical models and benchmarked against transient compressible simulations performed with the Lattice Boltzmann method (LBM). In section II, the description of the experimental setup and of the data-reduction techniques are presented. Section III focuses on the numerical test-case with the most relevant parameters for the computation. Section IV presents the experimental and computational results: the mean and turbulent velocity statistics, and the obtained pressure fields. Finally, section V concludes the discussion.

II. Experimental setup and data reduction

A. Wind tunnel model

A solid and a slitted trailing edge are retrofitted to a wing with a NACA 0018 airfoil. The model has chord length of $c = 200$ mm and a span of 400 mm (Figure 1). It is installed in the low-speed V-tunnel of Delft University of Technology. The open-jet wind-tunnel has a test-section of 400 mm \times 400 mm and it is operated at free-stream velocity of $V_\infty = 20$ m/s and free-stream turbulence intensity below 1%. The wing is set at angle of attack $\alpha = 0$. The boundary-layer is forced to turbulent transition by carborundum roughness elements of nominal grain size of about 0.589 mm randomly distributed over a 5 mm band along the entire span at $0.2c$ from the leading edge. The achievement of a uniform transition along the wing span is verified with the broadband response of a microphone probe downstream of the roughness elements.

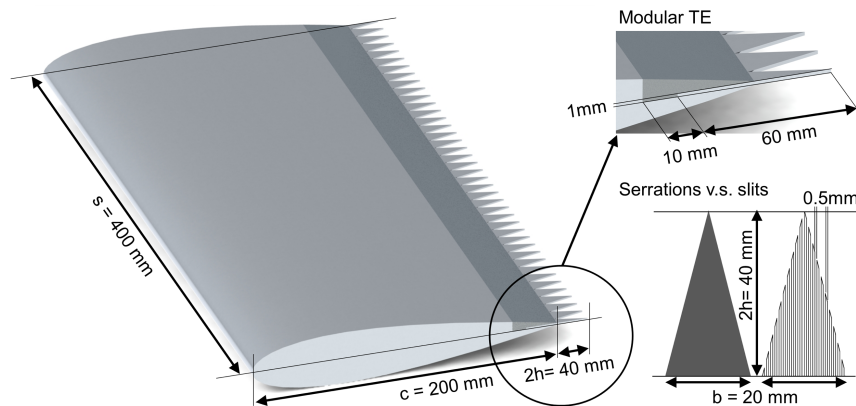


Figure 1. Wing, solid and slitted serration dimensions.

The wing has been manufactured using computer numerical-control machining from an aluminum block with a surface roughness down to 0.05 mm. A modular trailing-edge able to retrofit laser-cut serrations, slits elements as well as the original trailing-edge (STE, 1 mm thick edge) has been manufactured as shown in Figure 1. Both the solid and slitted serrations have length $2h=20\%c$ and wavelength $b=h$ (Sr20R21). Slits are obtained by laser cutting slots of 0.5 mm in the serrated shape. The serration length is chosen to be equal to four times the length of the boundary-layer thickness based on 95% of the free-stream velocity (δ_{95} , based on XFOIL¹⁹ computations) for the tested Reynolds number of 263,000.

A Cartesian coordinate system is defined in Figure 2 with its origin chosen at the mid-plane location of the wing trailing edge. Its z -axis coincides with the airfoil trailing edge itself, while the x -axis is aligned with the chord of the airfoil (i.e. aligned with the serration surface). It follows that the y -coordinate axis is orthogonal to the wing chord and to the surface of the installed add-ons.

B. Acoustic phase array

Microphone array measurements are employed to quantify the noise reduction capabilities of the adopted serration. An array with 64 microphones and of an effective diameter D of 0.9 m is used, arranged in a multi-arm

logarithmic spiral configuration as in the experiments of Arce Leon *et al.*⁸ The array is placed 1.26 m away from the airfoil in the direction normal to the mean camber plane of the airfoil. The center of the array is aligned in the stream wise direction with the root of the serrations at the trailing edge. The sampling frequency is 50 kHz, and the selected sound frequency range of interest extends from 1 to 5 kHz. For each measurement, a recording time of 60 s is employed. The acoustic data is averaged using time blocks of 2048 samples ($\Delta t = 40.96$ ms) for each Fourier transform and windowed using a Hanning weighting function with 50% data overlap. With these values, the frequency resolution for the source maps is 24.41 Hz. The averaged cross-spectral matrix required for beamforming is obtained after cross-correlating the microphones signals. The expected error²⁰ in the estimation of the cross-spectrum is 2.6%.

The rectangular scan grid used for beamforming covers the expected area of noise generation, ranging from $z = -0.22$ m to $z = 0.22$ m in the span wise direction and from $x = -0.7$ m to $x = 0.3$ m in the stream wise direction, according to the axes defined in Figure 2, with a distance between grid points of 1 mm. Therefore, the scan grid covers the whole airfoil and extends from the nozzle exit until 0.3 m after the trailing edge using 441×1001 grid points. The minimum angular distance at which two different sources can be separated using an array of circular aperture of diameter D can be estimated using the Rayleigh criterion. For the current experimental set-up, the minimum angular distance for the highest frequency considered in this analysis (5 kHz), considering $c = 340$ m/s, is $\phi = 0.092$ rad. Thus, the minimum resolvable distance, R , at a distance from the array r of 1.26 m is $R = r \tan \phi \approx 0.12$ m. Therefore, the selected spacing between grid points is approximately 120 times smaller than the Rayleigh's limit distance at that frequency.

Because trailing-edge noise is supposed to be a distributed sound source, the source maps are integrated over an area extending from $z = -0.1$ m to $z = 0.1$ m and from $x = -0.06$ m to $x = 0.06$ m. This section is chosen to minimize the contribution from extraneous sound sources, while still containing a representative part of the trailing edge.²¹ The beamforming results in that area are normalized by the value of the integral of a simulated point source of unitary strength placed at the center of the area of integration, evaluated within the same spatial boundaries.²² This process is then repeated for each frequency of interest to obtain the acoustic frequency spectra of the trailing edge.

Each microphone is previously calibrated using a pistonphone which generates a 250 Hz signal of known amplitude. Moreover, the performance of the array itself is assessed and calibrated by using tonal sound generated with a speaker at a known position emitting at several single frequencies: 500, 1000, 2000, 3000, 4000 and 5000 Hz. The SPLs at the center of the array are also measured with a calibrated TENMA 72-947 sound level meter. Therefore, the microphone array is calibrated in both source position and strength detection. The effect of the shear layer in the acoustic measurements is neglected due to the small angle between the center of the array and the scan area of interest and the considerably low flow velocities employed in this experiment.

C. Stereoscopic particle image velocimetry

Time-resolved stereoscopic PIV is employed to obtain both statistically independent and time-resolved velocity fields at the trailing-edge of the wing. A stereoscopic setup is realized by seeding the flow with tracer particles from an evaporated glycol-based SAFEX mixture with liquid droplets of about 1 μm . Illumination is provided by a *Quantronix* Darwin Duo laser (Nd:YLF, 2×25 mJ per pulse at 1 kHz). Laser optics formed a light sheet with a width of approximately 80 mm and a thickness of 1.5 mm.

A schematic of the time-resolved stereoscopic PIV field of view (FOV) is presented in Figure 2. Particle images are recorded by two *Photron* Fastcam SA1.1 CMOS cameras (1024×1024 pixels, 12 bit, 20 $\mu\text{m}/\text{px}$) equipped with a *Nikon-Nikkor* 105 mm focal-length macro-objective set at $f_{\#} = 5.6$. The stereoscopic setup features one camera displaced at 90° with respect to the free-stream velocity and a second one at an angle of 35° with respect to the first one. A Scheimpflug adaptor is used to focus the camera inclined with respect to the flow on the measurement plane. The final field of view is obtained by dewarping the images acquired by both cameras into a single field, subsequently calibrated with a multi-plane target. With an overall distance of about 40 cm from the middle plane, the resulting magnification factor is about 0.40. A resulting area of 2×5 cm^2 is obtained by cropping the sensor to 512×1024 px^2 , imaged at a digital resolution of about 20 px/mm . Stereoscopic PIV parameters are summarized in Table I.

Acquisition of the statistical data is obtained reducing the acquisition frequency to 250 Hz in order to obtain uncorrelated velocity fields. Time-resolved data are acquired by sequences of snapshots at a frequency of 5 kHz (frame separation of 200 μs) with a pulse separation time of 100 μs , further rearranged in a 10 kHz sequence (free-stream particle displacement of 24 px at 20 m/s). Illumination and imaging systems are synchronized by means of a *LaVision* HighSpeed Controller. The *LaVision* DaVis 8.1 software is used for acquisition and processing.

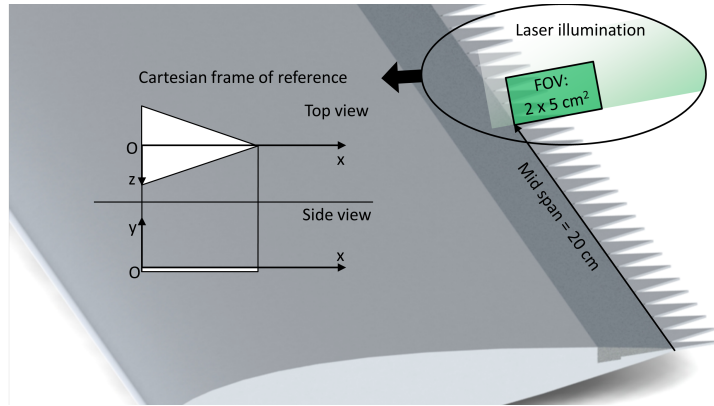


Figure 2. Schematic of the PIV plane and orientation of the Cartesian coordinate system.

Table I. Experimental parameters for the stereoscopic PIV setup

Parameter (TR acquisition)	Quantity
Imaging system	Photron Fastcam SA1.1
Frequency of acquisition	10 kHz
Δt between camera exposures	100 μ s
Acquisition sensor	512 \times 1024 pixels
Measurement area	20 \times 50 mm ²
Final interrogation window	16 \times 16 px ²
Overlap factor	75%
Digital resolution	20 px/mm
Magnification factor	0.40
Number of vectors	90 \times 170
Vectors resolution	0.8 \times 0.8 mm ²
Vector spacing	0.2 \times 0.2 mm ²
Free-stream pixel displacement	25 px

A multi-pass algorithm²³ with window deformation²⁴ is used to compute the velocity fields. Spurious vectors representing less than 5% of the total number, were tracked and removed by use of a median filter²⁵ with a kernel of 5 \times 5 vectors. A final interrogation window size of 16 \times 16 px² with an overlap factor of 75% is employed, resulting in a final resolution of 0.8 \times 0.8 mm² and a final vector spacing of 0.2 \times 0.2 mm². The removed vectors were linearly interpolated with the surrounding ones.

The main sources of uncertainty in the velocity fields for the described setup are peak-locking, finite spatial resolution, stereoscopic calibration and cross-correlation uncertainties. Errors due to peak-locking are quantified with the actual size of the particle on the sensor. To avoid peak-locking problems, defocusing is applied to the raw images by slightly displacing the focus plane from the laser one.²⁶ The procedure allows keeping the imaged particle on the sensor in the range between 1-1.5 px, obtaining a stochastic distribution of round-off errors in the computed velocity field. Absence of considerable peak-locking effects is a-posteriori verified by plotting the histogram of the round-off value of the particle vector-displacements with their integer values. Errors due to modulation with finite spatial resolution of the resulting velocity fields may also influence the measured flow structures. With the applied multi-pass cross-correlation algorithm and the application of window deformation, the length scale of flow structures measured with less than 5% modulation has to be larger than 1.7 times the window size.²⁷ Having a window size of 0.8 \times 0.8 mm², flow structures down to 1.2 mm can be measured with a 95% accuracy. Errors due to stereoscopic calibration are mitigated by an iterative self-calibration²⁸ procedure, applied to further improve the fitting of the dewarped images from the initial location to the calibration target plane. Random errors are mainly due to the cross-correlation algorithm and they have been found to vary with respect to the region of interest in the instantaneous vector fields; i.e. less than 1% error in the free-stream region and less than 3% in the inner boundary-layer one.²⁹ Quantification of the overall level of uncertainty when considering the size of the statistical sample the uncertainty on

the mean velocity is assessed to $0.05\%V_\infty$, and on the root-mean-square to $2\%V_\sigma$ where V_σ is the root-mean-square of the instantaneous values.

For the time-resolved evolution of the velocity fields a systematic error arises from the particle acceleration between the two exposures. Boillot & Prasad³⁰ quantifies this error as:

$$\epsilon_{u,sys} = \frac{1}{4} \Delta t \left\| \frac{DV_p}{Dt} \right\| \quad (1)$$

where DV_p/Dt is the measured particle velocity and Δt is the laser separation-time. With a measured average particle acceleration of about 7000 m/s^2 , the systematic error in the velocity fields is estimated to be about 1.7% of the free-stream velocity.

D. Evaluation of the pressure fluctuations

The flow pressure is computed from the Navier-Stokes momentum equation with the PIV velocity fields as input.³¹ When considering a stationary orthonormal Cartesian frame of axis x_i , with the respective velocity components u_i , the pressure gradient in Einstein's notation reads:³²

$$\frac{\partial p}{\partial x_i} = -\rho \frac{Du_i}{Dt} + \mu \frac{\partial u_i^2}{\partial x_j \partial x_j} = -\rho \left(\frac{\partial u_i}{\partial t} + u_j \frac{\partial u_i}{\partial x_j} \right) + \mu \frac{\partial u_i^2}{\partial x_j \partial x_j} \quad (2)$$

where i, j are Einstein's indices, p, ρ and μ are respectively the flow pressure, density and dynamic viscosity, while ∂ and D represent the partial and total flow derivatives. Analytically, equation 2 can be written either in function of the material acceleration D/Dt (Lagrangian formulation) or as combination of the temporal/spatial velocity derivatives (Eulerian formulation). Previous studies³³ demonstrated that the uncertainty on the material acceleration can be lowered by following a Lagrangian approach, where the consecutive velocity fields with temporal spacing Δt are used to track the motion of specific fluid particles in time. This particular approach has been followed in the present manuscript for the evaluation of the pressure gradient for the boundary conditions in the domain. The Laplacian of the pressure to be solved is independent from the time derivative on the inside of the domain. For incompressible flows:³²

$$\frac{\partial^2 p}{\partial x_i^2} = -\rho \frac{\partial}{\partial x_i} \left(u_j \frac{\partial u_i}{\partial x_j} \right) \quad (3)$$

Neumann conditions are applied in the rotational part of the domain, while Dirichlet conditions are applied in the outer part of the boundary layer.

III. Computational test case and solver

Comparison of the PIV data with respect to pressure fluctuations and spectra is carried out with 3D transient numerical simulations of the flow field. Special attention is given to the correct reproducibility of the boundary-layer integral parameters. Numerical computations are performed on a serrated NACA 0018 wing of chord $c = 200 \text{ mm}$. A span of $s = 80 \text{ mm}$ is simulated in order to encompass at least four full serrations. The domain size of the simulation is chosen to be $12c$ in both stream-wise and wall-normal directions in order to reach far-field boundary conditions. The outer $2c$ region is modeled as an anechoic outer-layer, for dampening of any unwanted acoustic reflections. In the span-wise direction periodic boundary-conditions are used instead. A variable mesh resolution in the computational field is employed with a grid-size change factor of two, resulting in a total of 10 refinement regions. The boundary-layer is represented by extra refinement regions allowing to place the first cell in the viscous sub-layer at $3.9 \times 10^{-4}c = 0.078 \text{ mm}$ above the trailing-edge location, corresponding to $y^+ = 3$. In total ~ 150 million voxels are used for discretization of the domain. Data sampling starts after reaching a steady standard deviation of the lift and drag coefficient, which corresponds to approximately 10 flow passes over the chord at 20 m/s . Imposition of a unitary Courant–Friedrichs–Lewy (CFL) number results in a computational time step of $1.3 \times 10^{-7} \text{ s}$. Flow data are stored at sampling frequency 7.7 kHz (time step of $1.3 \times 10^{-4} \text{ s}$). Surface pressure fluctuations are sampled at 30 kHz . The prescribed methodology was validated in a previous study by van der Velden *et al.*³⁴ The trailing-edge thickness in the simulation is equal to the one of the aluminum model (1 mm thickness), in order to minimize any tonal noise component due to vortex shedding ($t/\delta \approx 0.1$ where δ is the expected boundary-layer thickness at the tested Reynolds,

cfr. Table II).³⁵ Free-stream velocity and angle of attack are 20 m/s and 0° . Similarly to the adopted experimental model, boundary-layer transition to turbulence was forced at $0.2c$ by means of a serrated strip of height $3 \times 10^{-3}c$ (0.6 mm) and stream-wise length of $1.5 \times 10^{-3}c$ (0.3 mm) on both sides of the airfoil. For a statistical evaluation, the computed numerical results have been spatially averaged along different serrations due to the evident flow similarities over three serrations present in the computation domain, and to the beneficial reduction of the uncertainty.

The commercial software package *Exa* PowerFLOW 5.3b is used to solve the discrete Lattice Boltzmann equations in a finite number of directions. For a detailed description of the equations used for the source field computations the reader can refer to Succi.³⁶ More in detail, the discretization used for this particular application consists of 19 discrete velocities in three dimensions (D3Q19) involving a third-order truncation of the Chapman-Enskog expansion. The distribution of particles is solved using the kinetic equations on a Cartesian mesh, with the Bhatnagar-Gross-Krook (BGK) collision term operator.³⁷ A Very Large Eddy Simulation (VLES) is implemented as viscosity model to locally adjust the numerical viscosity of the scheme.³⁸ The model consists of a two-equation k - ϵ Renormalization Group (RNG) modified to incorporate a swirl-based correction that reduces the modeled turbulence in presence of large vortical structures. A turbulent wall-model is used to resolve the near-wall region.³⁹ The particular choice of both the turbulence model and wall model allow for a reliable estimate of the full boundary-layer parameters with feasible turn-around times.

IV. Results and discussion

A. Far-field noise measurements

Spectra of the far-field noise measurements obtained with the microphone array are plotted in Figure 3 for both the solid (left) and the slitted (right) serrations in one-third octave bands. They are presented in terms of difference of measured *SPL* (ΔSPL) with respect to the straight trailing-edge configuration. Positive ΔSPL means noise reduction. Data are obtained at V_∞ equal to 30, 35 and 40 m/s to guarantee high signal to noise ratio.

Measurements show the characteristic spectra of broadband noise without any tonal noise component due to vortex shedding. The solid trailing-edge serrations reduce noise more than the slitted one independently on the free-stream velocity. The maximum measured noise reduction is approximately 1.5 times larger for the solid serrated trailing edge. Furthermore, the frequency corresponding to the maximum ΔSPL is lower for the solid serration.

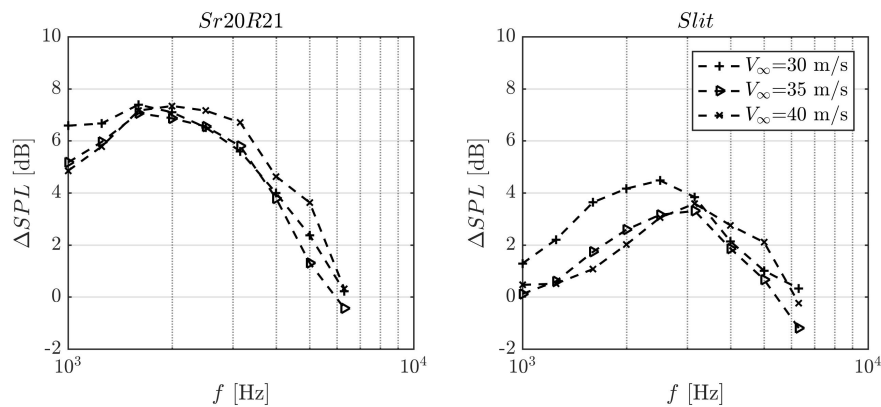


Figure 3. Difference in the measured sound pressure level (ΔSPL) with respect to the straight trailing-edge configuration for both the solid and slitted trailing edge. Positive means far-field noise reduction.

B. Turbulent boundary layer characterization and mean pressure field

The characterization and the assessment of the boundary layer is carried out by estimating the boundary-layer integral parameters at three locations along serration edge, as well as at the original straight trailing-edge location.

PIV results are presented in Figure 4, in terms of normalized mean velocity magnitude $|V|/V_\infty-1$ and pressure coefficient, expressed as mean \bar{c}_p and root mean-square c'_p of pressure fluctuations. Masked regions correspond to domains where the serrations impede the camera view. Pressure data are obtained as described in section II.C. The mean velocity contours (Figure 4, first row) show flow features pertaining to the boundary-layer development at the trailing edge of the airfoil. A mild pressure recovery is seen at the trailing edge which does not reach the free-stream value due to the presence of the viscous wake. Very small differences can be appreciated in the mean velocity field when changing both span-wise and stream-wise location, mainly due to the almost negligible pressure gradient at the trailing edge. When extending the comparison to the fluctuating pressure components slightly higher values are measured for the straight trailing edge with respect to the serrated case. The relatively small increase in fluctuations at the edge of the domain is due to the higher fluctuations due to the higher uncertainty of the PIV data (due to particles entering and leaving the domain).

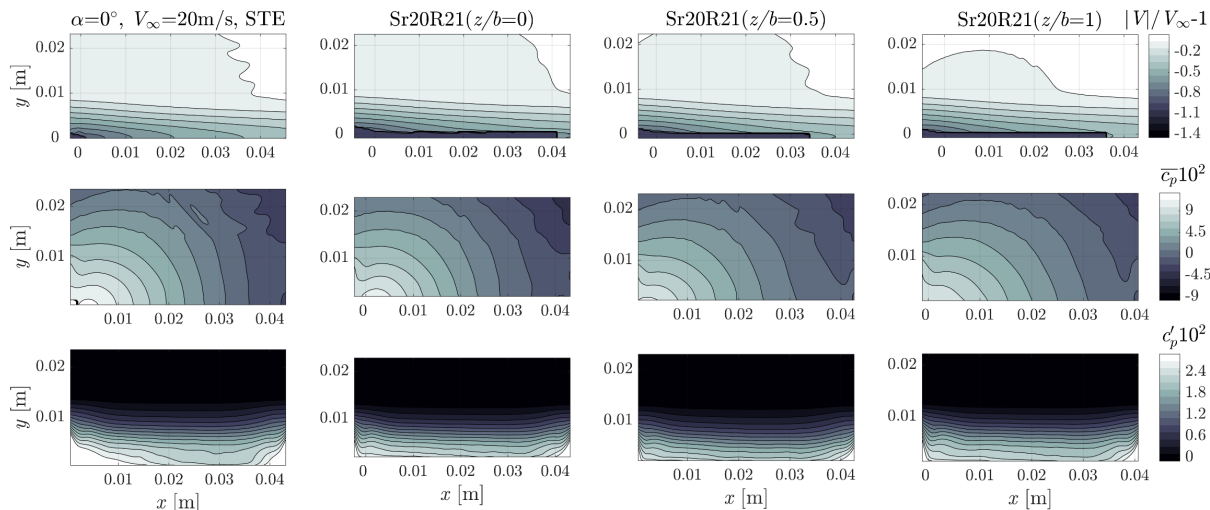


Figure 4. PIV fields organized in rows of normalized velocity magnitude ($|V|/V_\infty-1$), pressure coefficient (\bar{c}_p) and pressure coefficient fluctuations (c'_p). NACA 0018, $Re = 263,000$, $\alpha = 0^\circ$, $V_\infty = 20$ m/s. STE = straight trailing edge; Sr20R21 = serration with $2h = 20\%c$, and $2 \cdot h/b = 2/1$.

Table II. Boundary-layer characteristics estimated from planar PIV at $z/b = 1$; values corresponding to the un-serrated case STE ($x/c = 0$)

Parameter	Symbol	Quantity
Free-stream velocity	V_∞	20 m/s
Displacement thickness	δ^*	3.3 mm
Momentum thickness	θ	1.5 mm
Boundary layer thickness	δ_{99}	9.5 ± 0.1 mm
	δ_{95}	7.9 ± 0.1 mm
Reynolds number	Re_c	264,000
	Re_{δ^*}	4,500
	Re_θ	2,000
	Re_δ	13,200
Shape factor	H	2.2

Computation results are used to support the comparison with the experimental data especially in those regions where the PIV uncertainties are impeding reliable measurements (i.e. close to the surface). One of the most important aspects for a meaningful comparison between the two methods is the correct representation of the boundary-layer characteristics. In Figure 5, the mean normalized velocity magnitude, the boundary layer profile and the velocity fluctuations are plotted at the root of the serrated trailing edge and at the straight trailing edge location. Previous experimental studies showed that the incoming boundary layer at the trailing edge of the NACA 0018 serrated model at zero angle of attack is span-wise uniform and comparable to the one with no add-ons.⁸ This entails that the mean velocity profile at the root is also rather similar to the one of the un-serrated model, or equivalently that the upstream effect of the serrated geometry is rather limited. The boundary-layer profiles in Figure 5 confirm this evidence. The

boundary-layer parameters are additionally extracted from a line perpendicular to the airfoil surface at the trailing edge ($x/c = 0$) and summarized in Table II. The results from Figure 6 are used for comparison of the Reynolds stress and uncertainty analysis. A clear reduction of the Reynolds \overline{uu} component can be seen in presence of the solid serrations. This is in line with the experimental investigation from the authors,⁷ showing that even at zero angle of attack the mild acceleration experienced by the flow to adapt to the serration surface allows for a dampening of the stream-wise Reynolds fluctuations with respect to the straight case. For the test case comparing the both STE and Sr20R21 a reasonable agreement of the mean flow profiles and Reynolds stresses can be seen already from $y^+ = 20$ (corresponding to one window size for the PIV fields).

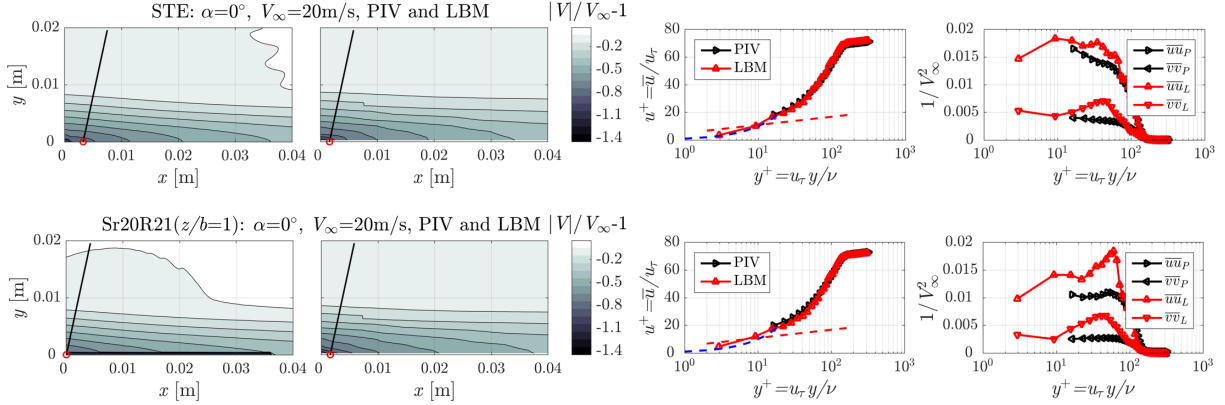


Figure 5. From left to right, normalized mean velocity magnitude ($|V|/V_\infty - 1$) from PIV (P) and LBM (L), velocity and Reynolds stresses profiles. NACA 0018, $Re = 263,000$, $\alpha = 0^\circ$, $V_\infty = 20$ m/s. STE = straight trailing edge; Sr20R21 = serration with $2h = 20\%c$, and $2 \cdot h/b = 2/1$. Dashed lines indicate the boundary-layer fit with log-law having constant $k = 0.39$, $B = 5$, $u_T = 0.23$ m/s.⁴⁰

C. Near-wall pressure distribution

The agreement between experiments and computations mean flow features guarantees the reproducibility of the results and allows further comparison of the mean and turbulent near wall pressure distribution. Figure 6 reports the mean and turbulent pressure along the wall-normal direction for the serrated case at the root location. In the following, data is normalized by the dynamic pressure $q_\infty = 1/2\rho V_\infty^2$, where the free-stream values are the respective values from the simulation and the experimental data (with approximately 7 Pa difference between the two). Both the numerical and experimental mean pressure-coefficient show similar pressure recovering at the trailing edge.

The maximum of the pressure fluctuations intensity is at about $y^+ = 50$, in the log-law region where also the profiles of the velocity fluctuations show a maximum. The shape and intensity of the overall static pressure fluctuations show a similar shape than the one computed assuming incompressible flow (i.e. using the Bernoulli equation). The latter are indeed obtained by first computing the total pressure in the free-stream P_T , and then by evaluating $\overline{p'^*} = \text{rms}[P_T - 1/2\rho(u^2 + v^2)]$. Similar values are found for the straight trailing edge configuration reported in Figure 7. In this case, a larger pressure recovery is seen close to the trailing edge. From the figure, it is evident that the intensity of the pressure fluctuations at the wall are approximately equal to the one measured at $y^+ \approx 20$. This corresponds to the beginning of the buffer layer.^{41,42} The flow viscosity seems to act by reducing the velocity fluctuations, still transferring pressure information from the outer layers.

In Figures 7 and 8 the comparison is shown for three locations along the serration edge. In Figure 8, each row reports relative magnitude of velocity, boundary-layer profiles, and Reynolds stresses. The pressure fluctuations are shown in Figure 9. Similarly to what already presented, these last ones are divided in terms of dynamic and static pressure fluctuations. Dashed lines in Figure 8 indicate the turbulent boundary-layer log-law. Results indicate a consistent change of the boundary layer profile along the serration. The departure from the original fit indicates a reduction of the boundary-layer thickness, induced by the acceleration determined by the presence of the serration.⁸ A decrease of the \overline{uu} components is again appreciated from the root to the tip, together with the vertical components \overline{vv} , though showing a smaller magnitude. When linking the present results with pressure fluctuations plots (Figure 9), a correspondence can be found between the location of maximum \overline{uu} and \overline{vv} , and of the one of maximum $\overline{p'}$.

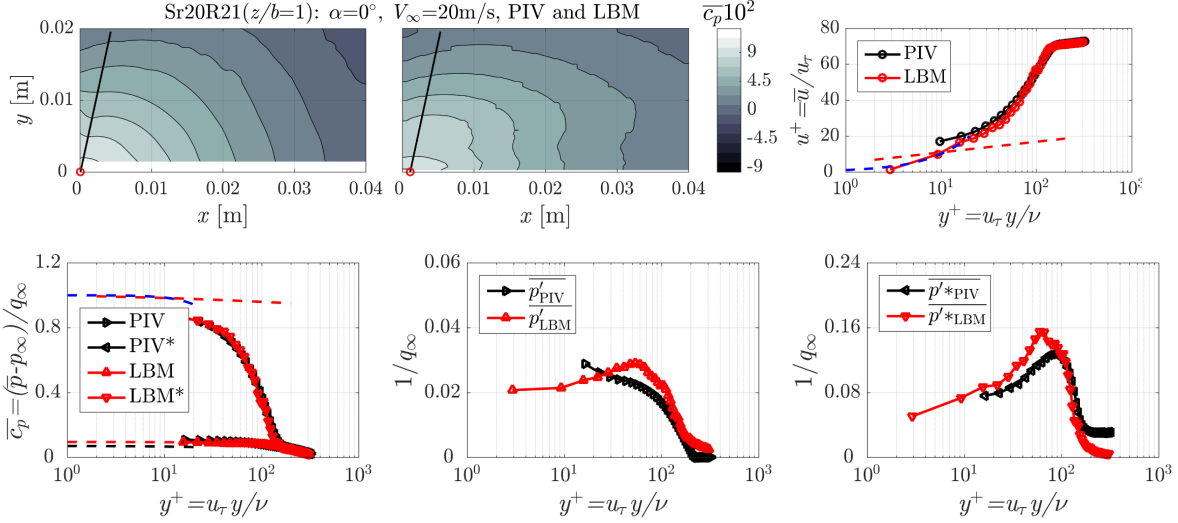


Figure 6. Top row: contours of mean pressure coefficient ($\overline{c_p}$) and boundary layer profile along the indicated solid line. Bottom row: mean pressure coefficient ($\overline{c_p}$) and time averaged pressure fluctuations ($\overline{p'}$). Time averaged isentropic pressure fluctuations ($\overline{p'^*}$) are added as reference. Data obtained from experimental PIV and LBM computations. NACA 0018, $Re = 263,000$, $\alpha = 0^\circ$, $V_\infty = 20 \text{ m/s}$. Sr20R21 = serration with $2h = 20\%c$, and $2 \cdot h/b = 2/1$. Dashed lines indicate the boundary-layer fit with log-law having constants $k = 0.39$, $B = 5$, $u_\tau = 0.23 \text{ m/s}$.⁴⁰

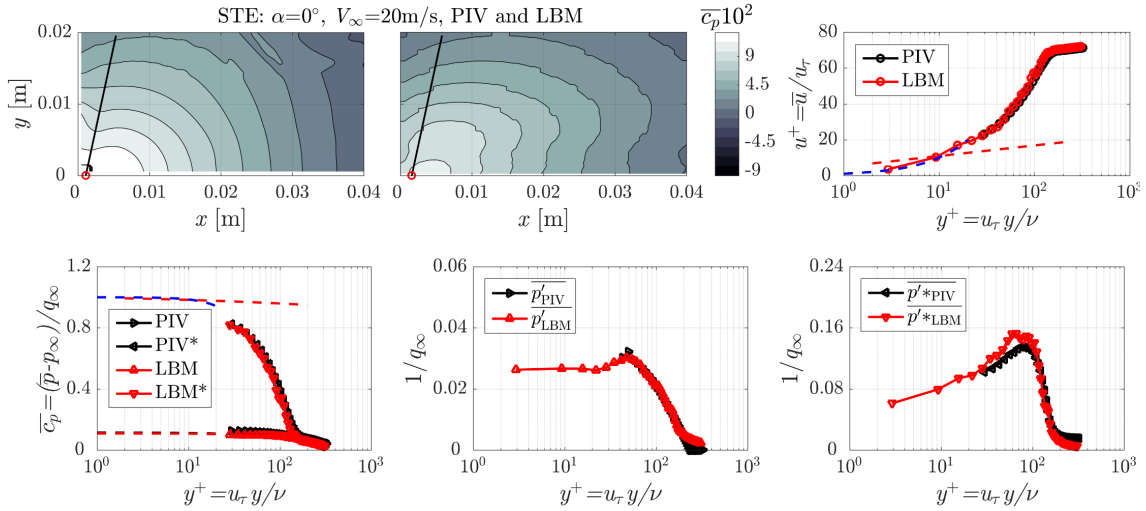


Figure 7. Top row: contours of mean pressure coefficient ($\overline{c_p}$) and boundary layer profile along the indicated solid line. Bottom row: mean pressure coefficient ($\overline{c_p}$) and time averaged pressure fluctuations ($\overline{p'}$). Time averaged isentropic pressure fluctuations ($\overline{p'^*}$) are added as reference. Data obtained from experimental PIV and LBM computations. NACA 0018, $Re = 263,000$, $\alpha = 0^\circ$, $V_\infty = 20 \text{ m/s}$. STE = straight trailing edge. Dashed lines indicate the boundary-layer fit with log-law having constants $k = 0.39$, $B = 5$, $u_\tau = 0.23 \text{ m/s}$.⁴⁰

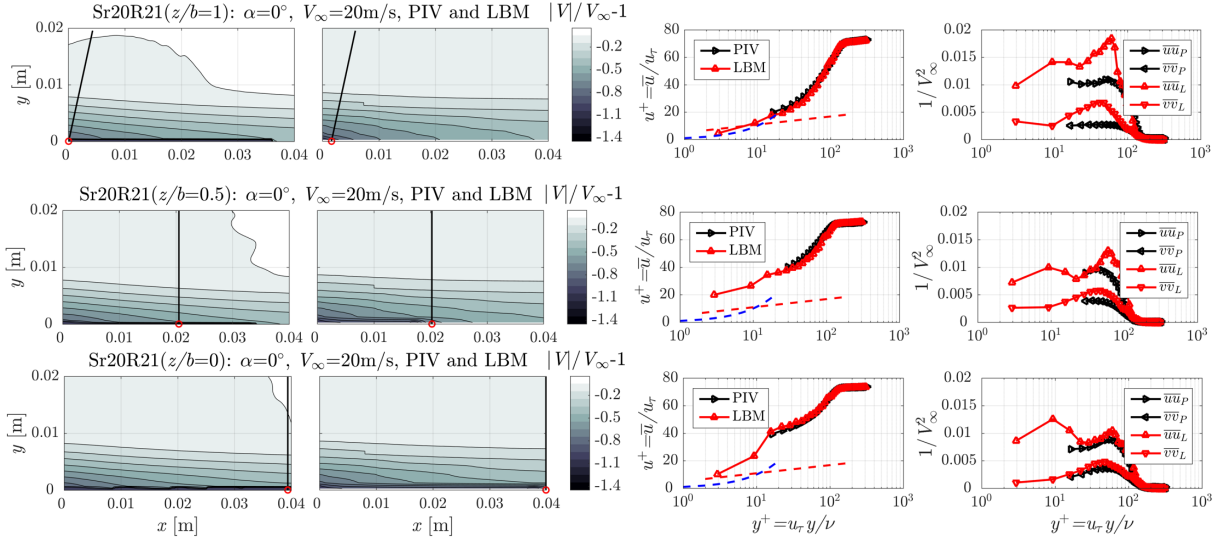


Figure 8. Comparison of relative magnitude of velocity, boundary layer profile and Reynolds stresses at three different stream-wise locations along the serration edge. Data obtained from experimental PIV and LBM computations. NACA 0018, $Re = 263,000$, $\alpha = 0^\circ$, $V_\infty = 20$ m/s. Sr20R21 = serration with $2h = 20\%c$, and $2 \cdot h/b = 2/1$. Dashed lines indicate the boundary-layer fit with log-law having constants $k = 0.39$, $B = 5$, $u_\tau = 0.23$ m/s.⁴⁰

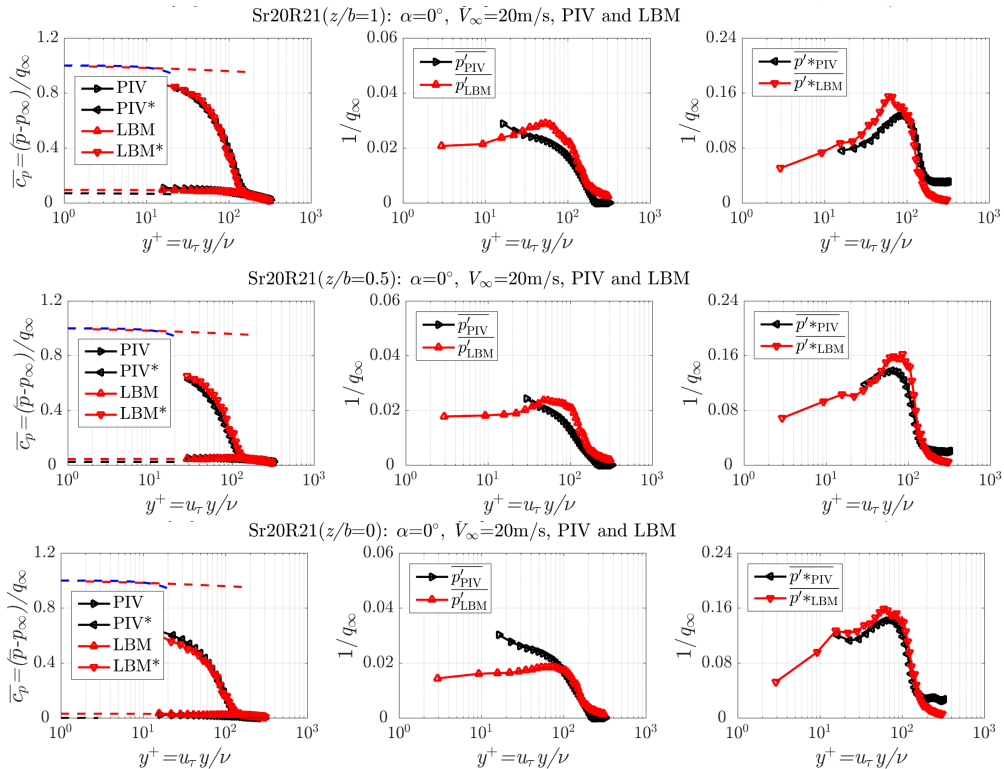


Figure 9. Mean pressure coefficient (\bar{c}_p), pressure fluctuations (\bar{p}') and Bernulli pressure fluctuations (\bar{p}'^*) at three different z locations along the edge of the solid serration. Data obtained from experimental PIV and LBM computations. NACA 0018, $Re = 263,000$, $\alpha = 0^\circ$, $V_\infty = 20$ m/s. Sr20R21 = serration with $2h = 20\%c$, and $2 \cdot h/b = 2/1$. Dashed lines indicate the \bar{c}_p obtained using the boundary-layer fit with log-law having constants $k = 0.39$, $B = 5$, $u_\tau = 0.23$ m/s.⁴⁰

The decrease in pressure fluctuation intensity is not due to the pure dynamic pressure (therefore velocity change) effect, since not visible from the Bernoulli-like pressure fluctuations. In summary results seem to point out that the presence of the triangular serrated shape has two major effects:

- 1) the creation of a span-wise periodic shear layer between the wake and the flow on top of the serration geometry which modifies the Reynolds stresses (i.e. fluctuations of velocity) and subsequently the surface pressure fluctuations;
- 2) the addition of a geometric surface with a specific skin-friction coefficient which allows variation of the pressure fluctuations magnitude along the area (and therefore serration edge).

These observations entail that the usage of a split plate could already lead to a positive noise reduction with respect to the conventional trailing-edge design of the blade. However, the more pronounced change of pressure fluctuations along the edge (observation 2) still allows the serration to be superior to the split plate in terms of noise-reduction performance.

D. Near-wall pressure spectra

In this section, spectra of the near-wall pressure fluctuations are discussed since essential for far-field noise estimation.¹³ Results are summarized in Figures 9 and 10. Although the spectra of the pressure fluctuations follow the conventional frequency decay of a turbulent boundary layer (cfr. -1, -7/3, -5/3 scaling), a clear mismatch at $z/b = 1$ between simulations and experiments is present. It is important to highlight that the spectra obtained from computations are on the surface while the ones derived from PIV are obtained at the closest location to the wall (at about 1 window-size, $y^+ = 20$) and normalized according to $\rho^2 V_\infty^3 \delta^*$. In Figure 11, different colors refer to spectra at three locations along the edge of the serration. Differently from the experiments, the numerical computations show a particular *cross-over* frequency, corresponding to a point where the pressure fluctuations at the edge become stronger (in frequency) than those ones from the straight trailing-edge configuration.

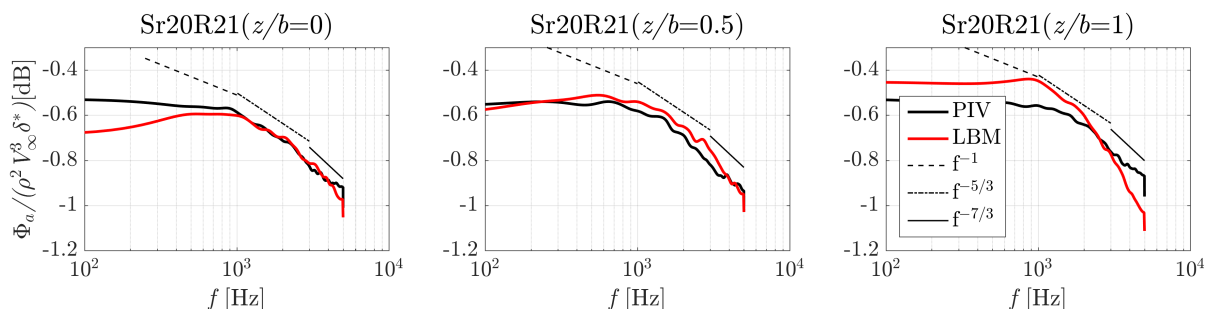


Figure 10. Spectra of the pressure fluctuations for different span-wise locations at the stream-wise locations of Figure 8. Values at the wall for the numerical (LBM) data while at $y^+ = 20$ for the experimental data. NACA 0018, $Re = 263,000$, $\alpha = 0^\circ$, $V_\infty = 20$ m/s. Sr20R21 = serration with $2h = 20\%c$, and $2 \cdot h/b = 2/1$.

A major target of the present investigation is indeed the study of the spatial change of the pressure spectrum along the serrated edge. This answer relies upon the type of turbulent boundary-layer that is generated at the trailing-edge of the serration. Although several studies have been accomplished with respect to modeling of the boundary-layer characteristics,⁴³ more recent improvement of predictions have been proposed by use of empirical laws⁴⁴ or by further refinement by Reynolds decomposition of the modeling.⁴⁵ In the present section, the model of Smolyakov & Tkachenko⁴⁴ is applied due to its high reliability when considering turbulent boundary-layers with low pressure gradient (as the one in this experiment). In Figure 12 the model is applied to the serrated edge by correcting each location with the actual parameters obtained along the serrated edge. Among the edge velocity, boundary-layer momentum thickness and skin-friction coefficient, the last one plays the most important role since it almost linearly changes along the edge. The skin friction coefficient as calculated from the experiment and the numerical simulations shows in fact a constant decrease till the tip of the serration (of a factor of about 3 from the root one). Once correcting for such a reduction, the data show a good collapse. From a physical point of view, the change of pressure fluctuations along the edge, that other studies reported as beneficial for noise reduction, can be modeled by obtaining a linear decrease of skin friction along the serration.⁷

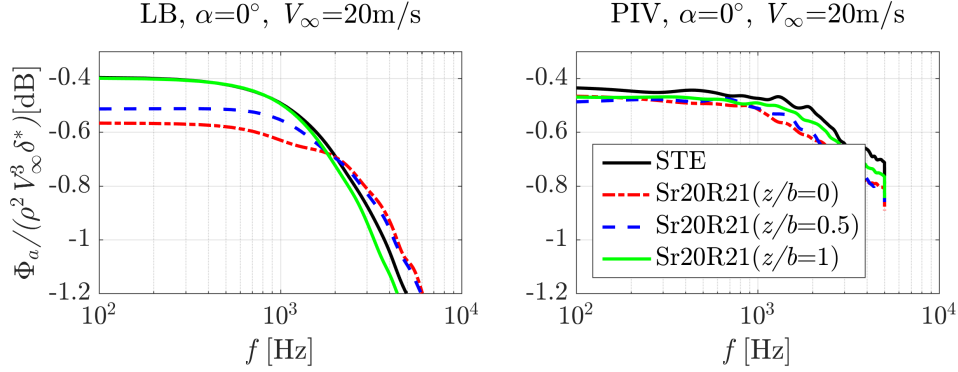


Figure 11. Spectra of the pressure fluctuations for different locations along the serration edge. Values at the wall for the numerical (LBM) data while at $y^+=20$ for the experimental data. NACA 0018, $Re = 263,000$, $\alpha = 0^\circ$, $V_\infty = 20$ m/s, Sr20R21 serration $2h=20\%c$ length, ratio = $2h/b = 2/1$.

Although studies from the same authors⁷ allow speculating on the beneficial effect given by the destructive interference of the scattered waves generated by such a rapidly changing pattern in pressure, further work is needed for a clear answer to this question. On the other side, the present manuscript quite remarkably states that those periodic shapes with a gradual change of “skin friction” (flow porosity) to their edge are favored in terms of noise reduction capabilities. Or equivalently, a *less abrupt* approach of the flow to the geometric discontinuity is indicating better performance in terms of lower noise emissions.

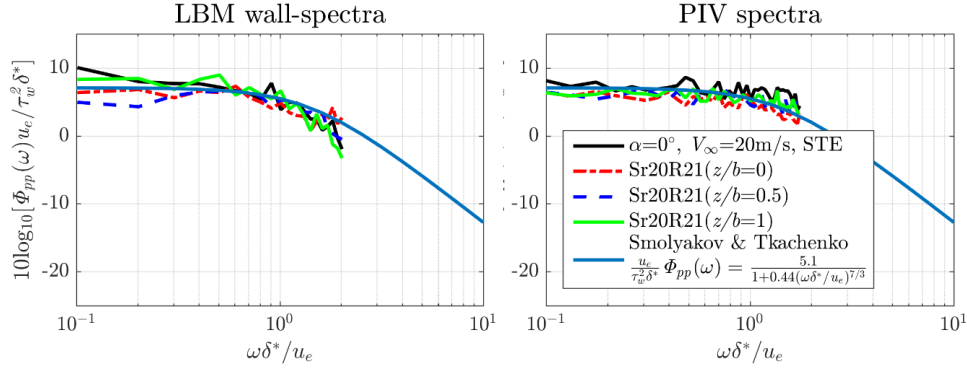


Figure 12. TBL-pressure modeling and scaling with respect to a linear change of friction coefficient along the serration. Values at for experimental PIV and numerical LB data: NACA 0018, $Re = 263,000$, $\alpha = 0^\circ$, $V_\infty = 20$ m/s, Sr20R21 serration $2h=20\%c$ length, ratio = $2h/b = 2/1$.

E. Comparison between slits and serrations

The previous section has pointed to the general trend that a distributed change of pressure fluctuations along the edge might be beneficial to noise reduction. In accordance with this statement, previous literature reported^{46,47} that modification of the solid serration into a slitted configuration (with a uniform porosity) does not always convey additional noise reduction benefits. On the other side, the combination of the two principles in the comb-serrated one⁶ showed more promising results due to the inclusion of the constant porosity in the empty space between the serration teeth. In the present section, having available velocity and pressure mean/fluctuations for both slitted and serrated trailing-edges, a comparison of the relative changes between the two can be made. In Figure 13 (top) a summary of the hydrodynamic changes is presented. As it can be seen from the contour plots, negligible differences are seen with respect to Figure 5 on both the levels of the pressure fluctuations and on their distribution. From a more detailed comparison between serrations and slits at their root, it can be deduced that the more porous surface sets a slightly

higher contribution of the pressure fluctuations at the root. This result may explain from a hydrodynamic point the behavior of many shapes realized by cut-out sleeves in a solid shape.⁴⁸ When plotting the surface pressure spectra in Figure 13-bottom, it can be seen that the pressure spectra at the root location more favorably compare to the ones measured with the STE configuration. In summary two main flow-effects are impeding the slits to out-perform their solid counterpart:

- 1) the triangular porous surface determines a weaker shear layer at the surface with respect to the one due to the solid surface;
- 2) the slitted roots promote higher pressure fluctuations (e.g. more similar to the straight edge ones) at their root.

It is therefore understandable that with respect to noise reduction, porous-periodic slit configurations are not more favorable than solid serrated ones.

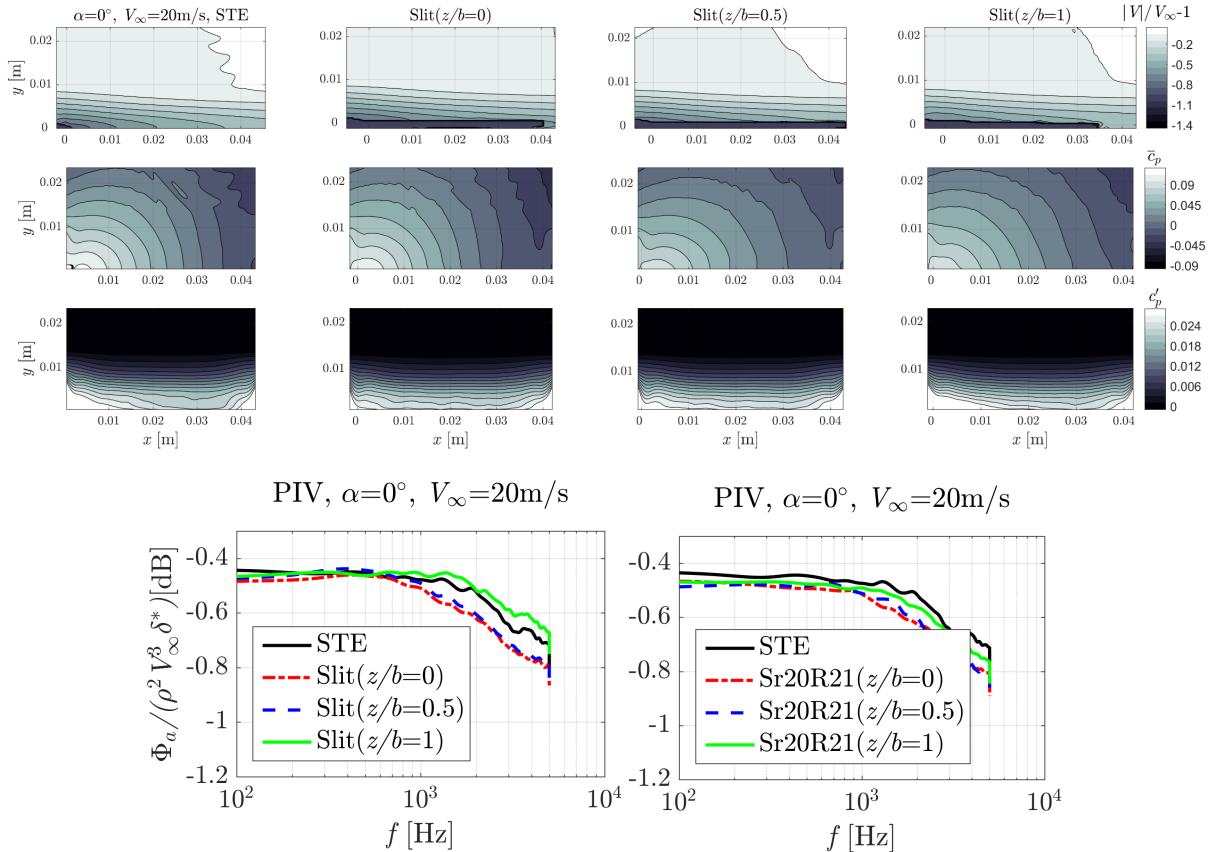


Figure 13. PIV fields organized in rows of: magnitude of mean velocity ($|V|/V_\infty-1$), pressure coefficient (\bar{c}_p) and pressure coefficient fluctuations (c'_p). Values at for experimental PIV: NACA 0018, $Re = 263,000$, $\alpha = 0^\circ$, $V_\infty = 20$ m/s, Slits and Sr20R21 serration with $2h=20\%c$, ratio = $2 \cdot h/b = 2/1$.

V. Conclusions

A study has been carried out to retrieve near-wall pressure along thin serrated edges. The present work has been focused on an experimental and computational test-case encompassing a NACA 0018 wing retrofitted with serrated and slits add-ons. Numerical computations from the Lattice-Boltzmann *Exa* PowerFlow 5.3b algorithm have been carried out by reproducing as close as possible the boundary-layer thickness as measured by time-resolved stereoscopic PIV at the edge of the serration. Results have shown a relatively good agreement between the PIV data and the Lattice Boltzmann ones. Once validated with the higher spatial and temporal resolution output of the numerical computations, results have been used to understand the role of the pressure fluctuations in the noise reduction

mechanisms of serrated devices. One of the major differences with respect to the analytical studies in literature has been found to be the change in the pressure fluctuation magnitude and spectra along the serration. This change can be represented with turbulent boundary-layer models (the one used in this manuscript is from Smolyakov & Tkachenko⁴⁴ for 0 angle of attack), where a change of skin-friction coefficient along the edge is considered (linear change along the serration edge to the wake in this manuscript). This conclusion opens new possibilities in terms of new periodic shapes which could be realized by employment of special paints or by combinations of slits and serrated edges as already seen in literature.⁶ The present study also shows that for slitted configurations, particular attention has to be devoted to the increase of the pressure fluctuations at the root, justifying the development of new shapes where the empty parts between the teeth are filled up.¹¹

Acknowledgments

The authors would like to thank Carlos Arce León and Dr. Stefan Pröbsting for participation in the experimental campaigns in the topic and in many discussions that brought to this work.

References

- ¹ Brooks, T. F., Pope, D. S., and Marcolini, M. A., *Airfoil self-noise and prediction*, National Aeronautics and Space Administration, Office of Management, Scientific and Technical Information Division, 1989.
- ² Brooks, T. F., and Hodgson, T. H., “Trailing edge noise prediction from measured surface pressures,” *Journal of Sound and Vibration*, vol. 78, Sep. 1981, pp. 69–117.
- ³ Lighthill, M. J., “On Sound Generated Aerodynamically. I. General Theory,” *Proceedings of the Royal Society of London A: Mathematical, Physical and Engineering Sciences*, vol. 211, 1952.
- ⁴ Oerlemans, S., Fisher, M., Maeder, T., and Kögler, K., “Reduction of Wind Turbine Noise Using Optimized Airfoils and Trailing-Edge Serrations,” *AIAA Journal*, vol. 47, May 2009, pp. 1470–1481.
- ⁵ Chong, T. P., and Vathylakis, A., “On the aeroacoustic and flow structures developed on a flat plate with a serrated sawtooth trailing edge,” *Journal of Sound and Vibration*, vol. 354, Oct. 2015, pp. 65–90.
- ⁶ Oerlemans, S., “Reduction of wind turbine noise using blade trailing edge devices,” *22nd AIAA/CEAS Aeroacoustics Conference*, Lyon, France: American Institute of Aeronautics and Astronautics, 2016, pp. 1–18.
- ⁷ Avallone, F., Pröbsting, S., and Ragni, D., “Three-dimensional flow field over a trailing-edge serration and implications on broadband noise,” *Physics of Fluids*, vol. 28, Nov. 2016, p. 117101.
- ⁸ Arce León, C., Merino-Martínez, R., Ragni, D., Avallone, F., and Snellen, M., “Boundary layer characterization and acoustic measurements of flow-aligned trailing edge serrations,” *Experiments in Fluids*, vol. 57, Dec. 2016, p. 182.
- ⁹ Chong, T. P., Joseph, P. F., and Gruber, M., “Airfoil self noise reduction by non-flat plate type trailing edge serrations,” *Applied Acoustics*, vol. 74, Apr. 2013, pp. 607–613.
- ¹⁰ Herr, M., and Dobrzynski, W., “Experimental Investigations in Low-Noise Trailing Edge Design,” *AIAA Journal*, vol. 43, 2005, pp. 1167–1175.
- ¹¹ Avallone, F., van der Velden, W. C. P., and Ragni, D., “Benefits of curved serrations on broadband trailing-edge noise reduction,” *Journal of Sound and Vibration*, vol. 400, 2017, pp. 167–177.
- ¹² Howe, M. S., “Noise produced by a sawtooth trailing edge,” *The Journal of the Acoustical Society of America*, vol. 90, 1991, pp. 482–487.
- ¹³ Lyu, B., Azarpeyvand, M., and Sinayoko, S., “Prediction of noise from serrated trailing edges,” *Journal of Fluid Mechanics*, vol. 793, Mar. 2016, pp. 556–588.
- ¹⁴ Gruber, M., Joseph, P. F., and Chong, T. P., “Experimental investigation of airfoil self noise and turbulent wake reduction by the use of trailing edge serrations,” *16th AIAA/CEAS Aeroacoustics Conference*, Stockholm, Sweden: American Institute of Aeronautics and Astronautics, 2010, pp. 1–23.
- ¹⁵ Ghaemi, S., and Scarano, F., “Multi-pass light amplification for tomographic particle image velocimetry applications,” *Measurement Science and Technology*, vol. 21, Dec. 2010, p. 127002.
- ¹⁶ Kraichnan, R. H., “Pressure Fluctuations in Turbulent Flow over a Flat Plate,” *The Journal of the Acoustical Society of America*, vol. 28, Jun. 1956, p. 378.
- ¹⁷ Blake, W. K., *Mechanics of Flow-Induced Sound and Vibration V2: Complex Flow-Structure Interactions, Volume 2*, Orlando, FL, Academic Press, Inc., 1986.
- ¹⁸ Stalnov, O., Chaitanya, P., and Joseph, P. F., “Towards a non-empirical trailing edge noise prediction model,” *Journal of Sound and Vibration*, vol. 372, Jun. 2016, pp. 50–68.
- ¹⁹ Dreila, M., “XFOIL: An Analysis and Design System for Low Reynolds Number Airfoils,” Springer Berlin Heidelberg, 1989, pp. 1–12.
- ²⁰ Brandt, A., *Noise and vibration analysis: signal analysis and experimental procedures*, Wiley, Hoboken, 2011.
- ²¹ Pagani, C. C., Souza, D. S., and Medeiros, M. A. F., “Slat Noise: Aeroacoustic Beamforming in Closed-Section Wind Tunnel with Numerical Comparison,” *AIAA Journal*, vol. 54, Jul. 2016, pp. 2100–2115.
- ²² Sijtsma, P., *Phased array beamforming applied to wind tunnel and fly-over tests*, 2010.
- ²³ Soria, J., “An investigation of the near wake of a circular cylinder using a video-based digital cross-correlation particle

- image velocimetry technique,” *Experimental Thermal and Fluid Science*, vol. 12, Feb. 1996, pp. 221–233.
- 24 Scarano, F., “Iterative image deformation methods in PIV,” *Measurement Science and Technology*, vol. 13, Jan. 2002, pp. R1–R19.
- 25 Westerweel, J., and Scarano, F., “Universal outlier detection for PIV data,” *Experiments in Fluids*, vol. 39, Aug. 2005, pp. 1096–1100.
- 26 Westerweel, J., “Fundamentals of digital particle image velocimetry,” *Measurement Science and Technology*, vol. 8, Dec. 1997, pp. 1379–1392.
- 27 Schrijer, F. F. J., and Scarano, F., “Effect of predictor–corrector filtering on the stability and spatial resolution of iterative PIV interrogation,” *Experiments in Fluids*, vol. 45, Nov. 2008, pp. 927–941.
- 28 Raffel, M., Willert, C. E., Wereley, S., and Kompenhans, J., *Particle Image Velocimetry - A Practical Guide*, Springer-Verlag Berlin Heidelberg, 2007.
- 29 Wieneke, B., “PIV uncertainty quantification from correlation statistics,” *Measurement Science and Technology*, vol. 26, Jul. 2015, p. 74002.
- 30 Boillot, A., and Prasad, A. K., “Optimization procedure for pulse separation in cross-correlation PIV,” *Experiments in Fluids*, vol. 21, Jun. 1996, pp. 87–93.
- 31 Baur, T.; Köngeter, J. ., “PIV with high temporal resolution for the determination of local pressure reductions from coherent turbulent phenomena,” *3rd Int. Workshop on Particle Image Velocimetry*, Santa Barbara: 1991, pp. 101–6.
- 32 Anderson Jr, J., “Fundamentals of Aerodynamics,” *Fundamentals of aerodynamics*, 1985, p. 982.
- 33 de Kat, R.; van Oudheusden, B. W. ., “Instantaneous planar pressure determination from PIV in turbulent flow,” *Experiments in Fluids*, vol. 52, May 2012, pp. 1089–1106.
- 34 van der Velden, W. C. P., Pröbsting, S., van Zuijlen, A. H., de Jong, A. T., Guan, Y., and Morris, S. C., “Numerical and experimental investigation of a beveled trailing edge flow and noise field,” *Journal of Sound and Vibration*, vol. 384, 2016, pp. 113–129.
- 35 Bearman, P. W., “Investigation of the flow behind a two-dimensional model with a blunt trailing edge and fitted with splitter plates,” *Journal of Fluid Mechanics*, vol. 21, Feb. 1965, p. 241.
- 36 Succi, S., *The lattice Boltzmann equation for fluid dynamics and beyond*, Oxford: Clarendon Press, 2001.
- 37 Bhatnagar, P. L., Gross, E. P., and Krook, M., “A Model for Collision Processes in Gases. I. Small Amplitude Processes in Charged and Neutral One-Component Systems,” *Physical Review*, vol. 94, 1954, pp. 511–525.
- 38 Chen, H., Kandasamy, S., Orszag, S., Shock, R., Succi, S., and Yakhot, V., “Extended Boltzmann Kinetic Equation for Turbulent Flows,” *Science*, vol. 301, 2003, pp. 633–636.
- 39 Chen, S., and Doolen, G. D., “Lattice Boltzmann method for fluid flows,” *Annual Review of Fluid Mechanics*, vol. 30, 1998, pp. 329–364.
- 40 White, F., *Viscous Fluid Flow*, McGraw-Hill Education, 2006.
- 41 Zagarola, M. V., Perry, A. E., and Smits, A. J., “Log laws or power laws: The scaling in the overlap region,” *Physics of Fluids*, vol. 9, 1997, p. 2094.
- 42 Barenblatt, G. I., and Shirshov, P. P., “Scaling laws for fully developed turbulent shear flows. Part 1. Basic hypotheses and analysis,” *J. Fluid Mech*, vol. 248, 2017, pp. 513–520.
- 43 Laufer, and John, “Investigation of Turbulent Flow in a Two-Dimensional Channel,” 1951.
- 44 Smolyakov, A. V., and Tkachenko, V. M., “Model of a field of pseudosonic turbulent wall pressures and experimental data,” *Soviet Physics-Acoustics*, vol. 37, 1991, pp. 627–631.
- 45 Peltier, L. J., and Hambric, S. A., “Estimating turbulent-boundary-layer wall-pressure spectra from CFD RANS solutions,” *Journal of Fluids and Structures*, vol. 23, Aug. 2007, pp. 920–937.
- 46 Arce León, C., Avallone, F., Pröbsting, S., and Ragni, D., “PIV Investigation of the Flow Past Solid and Slitted Sawtooth Serrated Trailing Edges,” *54th AIAA Aerospace Sciences Meeting, AIAA Scitech*, San Diego, California: American Institute of Aeronautics and Astronautics, 2016, pp. 1–15.
- 47 Gruber, M., Joseph, P. F., and Azarpeyvand, M., “An experimental investigation of novel trailing edge geometries on airfoil trailing edge noise reduction,” *19th AIAA/CEAS Aeroacoustic Conference*, Berlin, Germany: American Institute of Aeronautics and Astronautics, 2013, pp. 1–23.
- 48 Lyu, B., Azarpeyvand, M., and Sinayoko, S., “A Trailing-Edge Noise Model for Serrated Edges,” *21st AIAA/CEAS Aeroacoustics Conference*, Dallas, Texas: American Institute of Aeronautics and Astronautics, 2015, pp. 1–24.